nanomaterials

MDPI

Article

Mechanistic Investigation of the Formation of Nickel Nanocrystallites Embedded in Amorphous Silicon Nitride Nanocomposites

Norifumi Asakuma [1], Shotaro Tada [1], Erika Kawaguchi [1], Motoharu Terashima [1], Sawao Honda [1], Rafael Kenji Nishihora [2], Pierre Carles [2], Samuel Bernard [2] and Yuji Iwamoto [1,*]

[1] Department of Life Science and Applied Chemistry, Graduated School of Engineering, Nagoya Institute of Technology, Gokiso-cho, Showa-ku, Nagoya 466-8555, Japan; n.asakuma.633@stn.nitech.ac.jp (N.A.); tada.shotaro@nitech.ac.jp (S.T.); e.kawaguchi.310@stn.nitech.ac.jp (E.K.); m.terashima.311@stn.nitech.ac.jp (M.T.); honda@nitech.ac.jp (S.H.)

[2] CNRS, IRCER, UMR 7315, University of Limoges, F-87000 Limoges, France; rafael.nishihora@hotmail.com (R.K.N.); pierre.carles@unilim.fr (P.C.); samuel.bernard@unilim.fr (S.B.)

* Correspondence: iwamoto.yuji@nitech.ac.jp

Abstract: Herein, we report the mechanistic investigation of the formation of nickel (Ni) nanocrystallites during the formation of amorphous silicon nitride at a temperature as low as 400 °C, using perhydropolysilazane (PHPS) as a preformed precursor and further coordinated by nickel chloride ($NiCl_2$); thus, forming the non-noble transition metal (TM) as a potential catalyst and the support in an one-step process. It was demonstrated that $NiCl_2$ catalyzed dehydrocoupling reactions between Si-H and N-H bonds in PHPS to afford ternary silylamino groups, which resulted in the formation of a nanocomposite precursor via complex formation: Ni(II) cation of $NiCl_2$ coordinated the ternary silylamino ligands formed in situ. By monitoring intrinsic chemical reactions during the precursor pyrolysis under inert gas atmosphere, it was revealed that the Ni-N bond formed by a nucleophilic attack of the N atom on the Ni(II) cation center, followed by Ni nucleation below 300 °C, which was promoted by the decomposition of Ni nitride species. The latter was facilitated under the hydrogen-containing atmosphere generated by the $NiCl_2$-catalyzed dehydrocoupling reaction. The increase of the temperature to 400 °C led to the formation of a covalently-bonded amorphous Si_3N_4 matrix surrounding Ni nanocrystallites.

Keywords: Ni nanocrystallites; amorphous silicon nitride; nanocomposite; low temperature formation; polymer-derived ceramics

Citation: Asakuma, N.; Tada, S.; Kawaguchi, E.; Terashima, M.; Honda, S.; Nishihora, R.K.; Carles, P.; Bernard, S.; Iwamoto, Y. Mechanistic Investigation of the Formation of Nickel Nanocrystallites Embedded in Amorphous Silicon Nitride Nanocomposites. *Nanomaterials* **2022**, *12*, 1644. https://doi.org/10.3390/nano12101644

Academic Editor: Gabriela Mera

Received: 11 April 2022
Accepted: 10 May 2022
Published: 11 May 2022

1. Introduction

Transition metal (TM)-based compounds have been widely developed as heterogeneous catalysts in reactions involving energy-relevant transformations [1–3]. Growing interest in "sustainable growth", in industry and science as well as politics, still demands innovation to store, transmit, and/or convert any form of energy; thus, materials discovery appears to be a key element in the innovation cycle of energy conversion, transmission, and storage technologies [4].

Chemical routes toward ceramics are well-suited approaches for designing and synthesizing such highly active catalysts with the required ceramic robustness, especially in harsh environments. A very convenient precursor route is the polymer derived ceramics (PDCs) route, which allows fine control over the chemical composition of the final ceramic materials as well as their phase distribution and nanostructure [5–7]. In recent years, TM/Si-based (oxy-)carbide (SiC, SiOC) and carbonitride (SiCN) matrix nanocomposites, such as Ni/SiC, Ni/SiOC, Ni/SiCN(O), and M/SiCN (M = Pd, Ru, Pd_2Ru, Cu, Ir, Ni, Pt, Co, and Fe) derived from metal-modified polycarbosilanes, polysiloxanes, and polysilazanes

have been developed with enhanced catalytic performance and/or higher reusability [8–20]. Among them, as reported by Kempe et al., polymer-derived Ni/SiCN nanocomposites, while metal Ni is widely accepted as an active catalyst for hydrogenation/dehydrogenation reactions [21,22], are attractive as robust and reusable catalysts to be applied in the catalytic reactions for selective hydrogenation of nitroarenes.

Compared with M/SiCN nanocomposites, the design of M/Si-based nitride nanocomposites systems (i.e., M/Si_3N_4) is much more challenging, whereas the silicon nitride matrix could contribute to the catalytic activity of the whole system [23–28]. This might be due to the systematically thermodynamically-controlled formation of metal nitride through the reaction of the metal cations chemically-bonded and/or physically-loaded to the polysilazane with ammonia (NH_3), which is used as extrinsic nitrogen source for the formation of Si_3N_4. This is well illustrated in the recent reports on Si_3N_4-based nanocomposites, such as titanium nitride (TiN)/Si_3N_4 [29,30] and vanadium nitride (VN)/Si_3N_4 [31]. However, we recently succeeded in the formation of cobalt (Co)/Si_3N_4 nanocomposites through the PDCs route, using PHPS as amorphous Si_3N_4 (labeled a-SiN) precursor coordinated with $CoCl_2$ as Co source [32], although it was not possible to isolate samples free of ammonium chloride at low temperature while keeping the Si_3N_4 matrix amorphous, which is required for catalytic activity [27]. Moreover, the composites were synthesized in flowing NH_3, for instance, it was impossible to avoid the formation of ammonium chloride as a bi-product via the metal ammine chloride complex formation, especially at lower temperatures, which affected the in situ formation of nanocomposites.

In this study, the polymer-derived Ni/a-SN system has been selected for our synthetic investigation. This is expected to be essential to developing high-performance catalysts for hydrogenation/dehydrogenation reactions. Herein, we report the formation mechanism of Ni nanocrystallites surrounded by amorphous silicon nitride (a-SiN) free of ammonium chloride using PHPS as a-SiN precursor, further coordinated with $NiCl_2$ as Ni source. Moreover, inert nitrogen (N_2) atmosphere was applied for the present precursor pyrolysis to exclude the possibility of reactions of Ni-modified PHPS with atmospheric gas and to precisely monitor the intrinsic reactions during conversion of Ni-coordinated PHPS into Ni/a-SiN nanocomposite. The in situ formation of metallic Ni nanocrystallites within the polymer-derived a-SiN matrix was monitored by using a complete set of characterization techniques, including infrared spectroscopy, thermogravimetric–mass spectrometric (TG-MS) analysis, elemental analysis, powder X-ray diffraction (XRD), transmission electron microscopy (TEM) observation, and Raman spectroscopy. Thus, this study paves the way for the design of Ni/a-SiN nanocomposites, which can be applied in a wide range of catalysis-assisted reactions requiring harsh conditions.

2. Materials and Methods

2.1. Synthesis of Single Source Precursor for SiNiN System

Commercially available perhydropolysilazane (PHPS, NN120-20, 20 wt% in dibutyl ether solution, Sanwa Kagaku, Corp., Shizuoka, Japan) and nickel chloride ($NiCl_2$, 98% purity, Sigma-Aldrich Japan, Tokyo, Japan) were used without further purification. All the reactions and handling of the chemicals for precursor syntheses were carried out under an inert atmosphere of pure argon (Ar), using standard Schlenk line and grove box techniques. The dibutyl ether solvent of as-received PHPS was substituted by super-anhydrous toluene (99.5% purity, Wako Pure Chemical Industries, Ltd., Osaka, Japan) to be 20 wt% for the PHPS contents. Then, the synthesis of Ni-modified PHPS samples was performed at the atomic ratios of Ni in $NiCl_2$ to Si in PHPS (Ni/Si) = 0.05 and 0.2. The synthesized precursors were labeled as **0.05NiPHPS** and **0.2NiPHPS**, respectively. In a typical experiment, a 300 mL two-neck, round-bottom flask equipped with a magnetic stirrer was charged with the PHPS (20 wt% toluene solution, 21 mL, 93.1 mmol), then $NiCl_2$ (0.564 g, 4.44 mmol, Ni/Si = 0.05) and anhydrous toluene (20 mL) were added to the solution at room temperature. The resulting orange-colored solution was refluxed for 15 h under flowing Ar with stirring. During refluxing, the color of the solution

changed from orange to brown-gray. After the reaction mixture was cooled down to room temperature, the solvent was removed under vacuum at 50 °C to give Ni-modified PHPS (**0.05NiPHPS**).

2.2. Conversion to Ni/Amorphous SiN Composite

The **0.05NiPHPS** was subsequently pyrolyzed in a quartz tube furnace (Model FUW220PA, Advantec Toyo Kaisha, Ltd., Chiba Japan) under flowing N_2 (200 mL/min) up to specific temperatures of 200, 300, and 400 °C with the ramping rate of 5 °C min^{-1}. Then, each sample was quenched without holding time to afford Ni nanoparticle-dispersed amorphous silicon nitride composite sample labeled as **Ni/SiNX** (*X* represents the pyrolyzed temperature). As a reference, Ni-free PHPS was also pyrolyzed under the same manner to give amorphous silicon nitride sample denoted as **SiNX**. To study the Ni-nanoparticle formation within the PHPS-derived amorphous Si-N network, pyrolysis of as-received $NiCl_2$ alone was performed under flowing NH_3 or 10% H_2/Ar (200 mL/min) with the ramping rate of 5 °C min^{-1}. When the furnace temperature reached 300 °C, the flowing gas was switched from the reductive gas to N_2 before quenching as mentioned above.

2.3. Characterization

The synthesized single source precursors were characterized by an attenuated total reflection flourier transform infra-red (ATR-FTIR) spectroscopy using FTIR spectrometer (FT/IR-4200IF, JASCO Corporation, Tokyo, Japan) with a diamond prism under an incidence angle of 45° loaded in an ATR attachment (ATR PRO 550S-S/570S-H, JASCO Corporation, Tokyo, Japan). The ATR-FTIR spectra were collected at a resolution of 4 cm^{-1} with a cumulative number of 128 and the spectra were normalized by the strongest peak in the measured region.

To investigate the chemical bonding states, Raman spectra were recorded on pyrolyzed samples and as-synthesized samples (Model inVia, Renishaw, UK) using a single mode solid laser with wavelength 633 nm and power 25 mW for Raman excitation. The Raman spectra were also normalized by the strongest peak.

The thermal behavior up to 800 °C of as-received PHPS and **0.05NiPHPS** was studied by simultaneous thermogravimetric (TG) and mass spectroscopic (MS) analyses (Model STA7200, Hitachi High Technologies Ltd., Tokyo, Japan) coupled with a quadrupole mass–spectrometry (Model JMS-Q1050GC, JEOL Ltd., Tokyo, Japan)]. The measurements were performed under flowing He (100 mL/min) with a heating rate of 10 °C min^{-1}.

The chemical composition of the pyrolyzed samples was calculated according to following equation:

$$wt\%(\mathrm{Si}+\mathrm{Ni}+\mathrm{Cl}) = 100\% - wt\%(\mathrm{C}) - wt\%(\mathrm{N}) - wt\%(\mathrm{O}) \quad (1)$$

where the carbon (C) content was measured using a carbon analyzer (non-dispersive infrared method (Model CS844, LECO Corporation, MI, USA), and the oxygen (O) and nitrogen (N) contents were measured using an oxygen nitrogen hydrogen analyzer (inert gas fusion method, Model EMGA-930, HORIBA, Ltd., Kyoto, Japan), while the Si, Ni, and Cl contents were analyzed by the energy dispersive X-ray spectroscopy (EDS) mounted on a scanning electron microscope (SEM, Model JSM-6010LA, JEOL Ltd., Tokyo, Japan).

The powder X-ray diffraction (XRD) pattern analysis of the pyrolyzed samples was performed on a flat sample stage using Ni-filtered CuKα radiation (Model X'pert, Philips, Amsterdam, The Netherlands). XRD patterns were collected twice with two different scan rates: 4.7 and 0.8° min^{-1} in the regions of 10 to 90° and 35 to 55°, respectively. The average crystallite size (L) of metal nickel formed in situ, was obtained from the Scherrer equation as follows:

$$L = K\lambda/\beta\cos\theta \quad (2)$$

where λ is the X-ray wavelength in nanometer, K is a constant related to crystallite shape, generally applied as 0.9, and β is the peak width of the diffraction peak at half maximum height in radian. The β in this study was collected from the diffraction peak at 44.5° measured at the scan rate of 0.8° min^{-1}.

Transmission electron microscope (TEM) observations and high-angle annular dark-field scanning transmission electron microscope (HAADF-STEM) observations were performed on the pyrolyzed samples in a JEOL JEM-ARM200F operated at an accelerating voltage of 200 kV. The size of the electron probe was approximately 0.1 nm. The convergent angle and the detector collection angle were 22 mrad and 68–280 mrad, respectively. The Ni average size and size distribution histogram were obtained by measuring 50 particles in their longer direction using ImageJ program (NIH free software ver.1.52a).

3. Results and Discussion

3.1. Chemical Structure of Ni-Modified PHPS

To investigate the chemical bonding states of Ni-modified PHPS, ATR-FTIR spectroscopic analysis was performed on two samples, namely **0.05NiPHPS** and **0.2NiPHPS**, which display the Ni:Si atomic ratio of 0.05 and 0.2, respectively. As-received PHPS—who served as a reference—(black line in Figure 1a) presents typical absorption bands at 3372 (νN-H), 2143 (νSi-H), 1172 (δN-H), and 831 cm^{-1} (νSi-N-Si) [33,34]. Although Ni-modified PHPS samples show similar spectra (red and blue lines in Figure 1a), the relative absorption intensity of δN-H at 1172 cm^{-1} to νSi-N-Si ($A_{N\text{-}H}/A_{Si\text{-}N\text{-}Si}$) and that of νSi-H at 2143 cm^{-1} to νSi-N-Si ($A_{Si\text{-}H}/A_{Si\text{-}N\text{-}Si}$) decreased with the increase of the Ni/Si atomic ratio (Table S1). In addition, Ni-modified PHPS samples show shifts of νSi-N-Si band towards the lower wavenumber from 831 to 820–809 cm^{-1}, and the shifts increase consistently with the increase of the Ni/Si atomic ratio; thus, with the increase of the Ni content (Figure 1b).

It has been reported that the catalytic formation of bonds between Group 14 and Group 15 elements, such as Si-N bonds resulting from the dehydrocoupling reaction between Si-H and N-H, could be conducted in the presence of various transition metal compounds at the temperature ranges of 20–90 °C [35]. Considering our synthesis conditions (i.e., precursor synthesis conducted in toluene at reflux (~110 °C)), the $NiCl_2$-catalyzed dehydrocoupling reactions of Si-H/N-H are expected to proceed in our system to form further Si-N bonds.

Generally, the frequency of vibration (harmonic-oscillator) is inversely proportional to the square root of the mass of vibrating moiety. For instance, Lucovsky et al. reported that the Si-N stretching band attributed to $(\equiv Si)_3Si\text{-}N=$ was identified at a lower wavenumber in comparison with $(\equiv Si)_2HSi\text{-}N=$, in which one of the silicon moieties (≡Si) was replaced with a H atom [36]. The shift of νSi-N-Si band in Ni-coordinated PHPS toward lower wavenumber is—in this analogy—due to the occurrence of dehydrocoupling reactions catalyzed by $NiCl_2$ leading to the formation of ternary silylamino group ($(\equiv Si)_3N:$).

Based on these observations, the Ni-modified PHPS synthesized in this study can be characterized as follows: the ternary $(\equiv Si)_3N:$ group formed in situ via the $NiCl_2$-catalyzed dehydrocoupling reaction between the $(\equiv Si)_2HN:$ group and the H-Si≡ bond is suggested as a possible ligand that coordinates on the Ni(II) cation of $NiCl_2$ to afford a complex structure such as a 4-coordinate Ni(II) complex (Scheme 1).

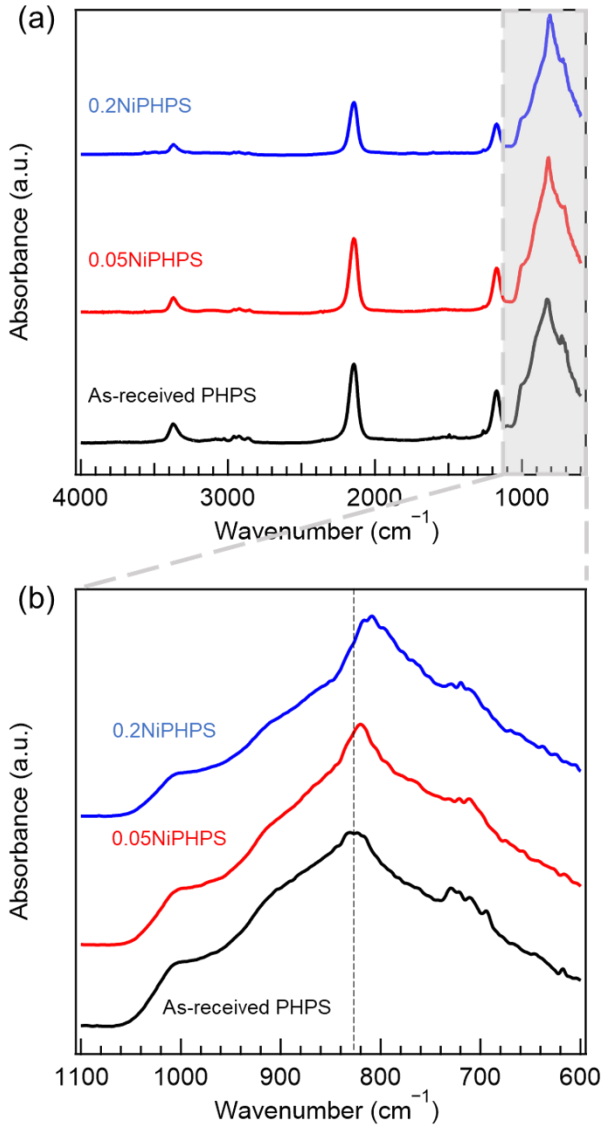

Figure 1. ATR-FTIR spectra of as-received PHPS (black line) and Ni-modified PHPS samples (red and blue lines represent the Ni/Si atomic ratios of 0.05 and 0.2, respectively): (**a**) 600–4000 cm^{-1} and (**b**) 600–1100 cm^{-1}.

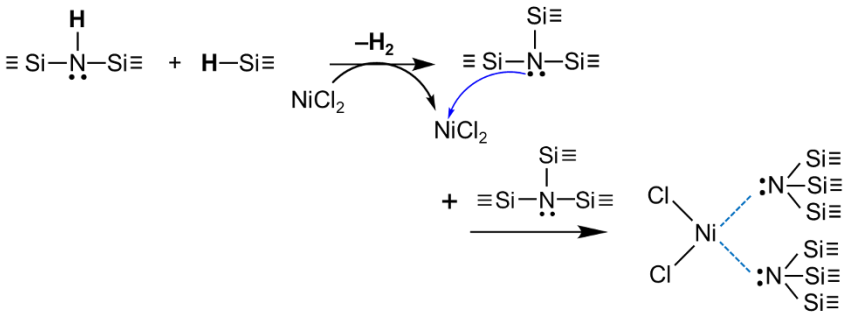

Scheme 1. Dehydrogenation reaction of Si-H/N-H in PHPS catalyzed by $NiCl_2$ and possible Ni(II) coordination structures, such as 4-coordinate Ni(II) complex.

3.2. Chemical Reaction during in Situ Nano Structuring Process

The occurrence of these mechanisms affects the ceramic conversion of PHPS. Therefore, the thermal behavior of the **0.05NiPHPS** sample has been monitored using TG-MS analysis

under flowing inert gas (He). The TG-curve and total ion current chromatogram (TICC) (Figure 2a) indicate that the weight loss contentiously occurs at 150 to 800 °C associated with the evolution of gas species in three temperature ranges as revealed by the simultaneous MS analyses (Figure 2b–e). They show that the weight loss up to 200 °C is due to the evaporation of residual reaction solvent as the evolved species are attributed to toluene ($C_6H_5CH_3$, m/z = 91, 92, Figure 2b), while at 200 to 800 °C, the weight loss can be divided into two regions based on the dominant species detected:

1. 200–480 °C: ammonia (NH_3, m/z = 16, 17, Figure 2c) and monochlorosilane (SiHCl, m/z = 64, 66, Figure 2d).
2. 480–800 °C: hydrochloric acid (HCl, m/z = 36, 38, Figure 2e).

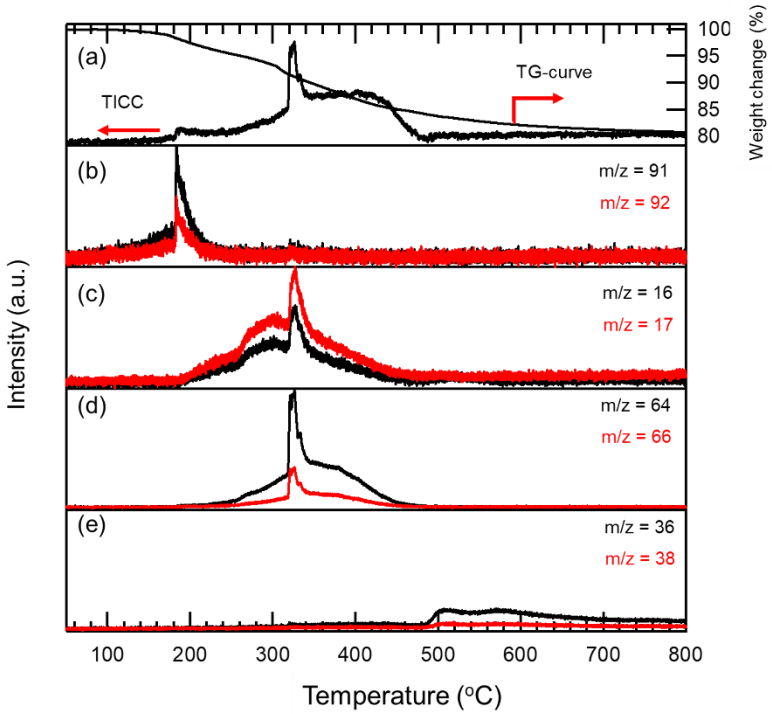

Figure 2. TG-MS analysis under flowing He of the **0.05NiPHPS** sample: (**a**) TG-curve coupled with the total ion current chromatogram (TICC), (**b**–**e**) the simultaneous monitoring of gaseous products formed in situ.

The release of NH_3 is due to the transamination reaction which is one of the typical cross-linking reactions occurring in polysilazanes [37,38]. Interestingly, the transamination reaction in **0.05NiPHPS** sample, i.e., within the cross-linked PHPS polymer network by the $NiCl_2$ modification (Figure 2), was found to proceed approximately 50 °C lower than that in the as-received PHPS sample (Figure S1).

The identification of monochlorosilanes and HCl is most probably due to the reaction between the Si center and/or NH units of PHPS with $NiCl_2$ that could form a nitride phase.

To investigate the transformation of Ni-modified PHPS samples into ceramics in more depth, we selected the **0.05NiPHPS** sample to be pyrolyzed at intermediate temperatures (200, 300, and 400 °C) under an inert gas (N_2) atmosphere. Then, the pyrolyzed intermediates labeled **Ni/SiNX** —with **X** the temperature at which the sample has been exposed— have been characterized by elemental analyses, X-ray diffraction, and Raman spectroscopy.

Table 1 lists the chemical compositions of the pyrolyzed samples (**Ni/SiNX**) along with those of PHPS-derived amorphous silicon nitride samples (**SiNX**) isolated at the same temperatures. At first, the Ni:Si ratio fixed in the early stage of the process, at the polymer level, increased during the pyrolysis indicating the release of Si-containing species, such as monochlorosilane, as identified by TG-MS (Figure 2). To support this observation, the N/Si and Cl/Si atomic ratios in **Ni/SiNX** samples decrease with the pyrolysis temperature

increase, which is consistent with the evolution of NH_3 and monochlorosilane, as shown during TG-MS analysis (Figure 2).

Table 1. Chemical composition of pyrolyzed samples.

	Composition/wt%						**Composition/at%**
	EDS (Ni/Si, Cl/Si Ratio)			**Elemental Analysis /wt%**			
Name	Si	Ni	Cl	C	N	O	Atomic ratio to Si
SiN200	71.58	-	-	1.01	23.65	0.33	$Si_1C_{0.03}N_{0.66}O_{0.01}$
SiN300	74.29	-	-	0.55	21.55	0.33	$Si_1C_{0.02}N_{0.58}O_{0.01}$
SiN400	76.98	-	-	1.08	18.70	0.40	$Si_1C_{0.03}N_{0.49}O_{0.01}$
Ni/SiN200	66.32	7.94	7.11	1.05	19.99	1.67	$Si_1Ni_{0.06}Cl_{0.08}C_{0.04}N_{0.60}O_{0.04}$
Ni/SiN300	66.48	10.62	3.62	0.96	17.44	1.44	$Si_1Ni_{0.08}Cl_{0.04}C_{0.03}N_{0.53}O_{0.04}$
Ni/SiN400	68.10	11.26	2.54	1.21	15.68	1.08	$Si_1Ni_{0.08}Cl_{0.03}C_{0.04}N_{0.46}O_{0.03}$

3.3. Chemical Composition of Nanocomposites

The XRD analysis reveals that Ni(II) keeps the initial state as dichloride at 200 °C (**Ni/SiN200** sample) since the diffraction pattern composed of the three peaks (2θ = 15.1, 32.8, 52.6°) completely matches the three main peaks detected for the $NiCl_2$ used in this study (Figure S2). Then, at 200 to 300 °C, the nucleation of metal Ni (JCPDS No. 01-070-1849, 2θ = 44.5, 51.8, 76.5°) proceeds and the corresponding XRD peaks are associated with those of the secondary phases, such as NH_4NiCl_3 (JCPDS No. 00-020-0098, 2θ = 14.7, 33.4, 40.0, 42.9°) and a trace amount of NH_4Cl (JCPDS No. 01-077-2352, 2θ = 32.8°, **Ni/SiN300** sample). At 400 °C (**Ni/SiN400** sample), the XRD peaks of byproducts disappear and metal Ni becomes the unique single crystalline phase identified in the XRD pattern (Figure 3a,b). It should be noted that Ni nanocrystallite cannot be formed by pyrolysis of pure $NiCl_2$ powder under reductive H_2 or NH_3 conditions, as well as in inert N_2 conditions (Figures S2 and S5). Therefore, it is strongly suggested that the Ni nanocrystallites are formed in situ through chemical reactions of PHPS with $NiCl_2$ leading to the formation of a covalently-bonded amorphous Si_3N_4 matrix surrounding Ni nanocrystallites.

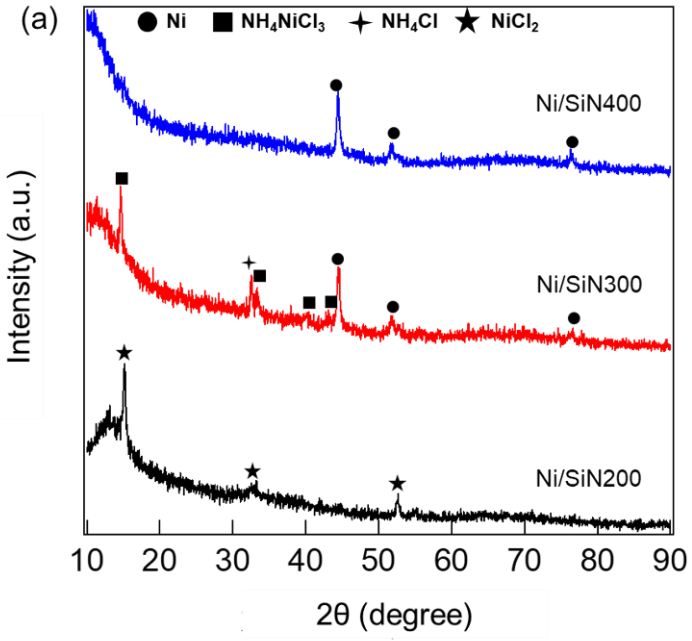

Figure 3. *Cont.*

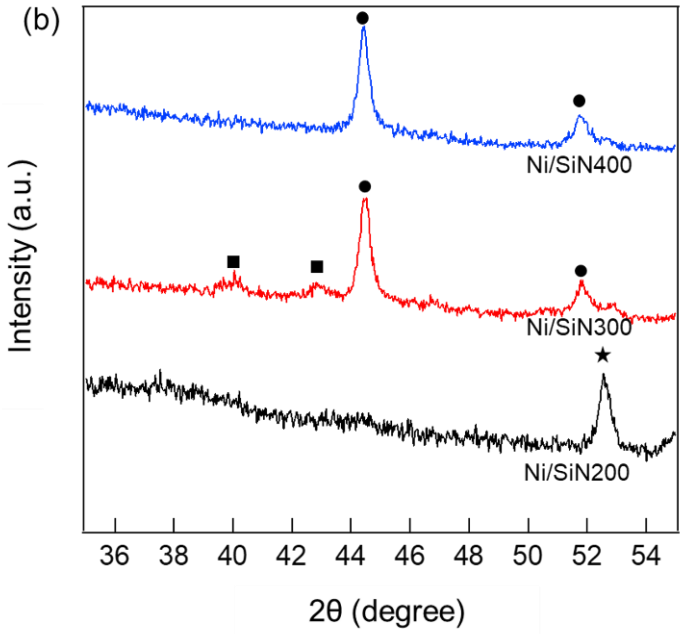

Figure 3. Powder X-ray diffraction patterns of **Ni/SiNX** samples pyrolyzed at 200, 300, 400 °C: 2θ = (**a**) 10–90° and (**b**) 35–55°.

The average crystallite size was calculated for the Ni (111) plane by using the Scherrer equation, and the initial average crystallite size at 300 °C of 18.4 nm was evaluated for the **Ni/SiN300** sample, then the crystallite size reached 18.5 nm at 400 °C (**Ni/SiN400** sample).

3.4. Mechanistic Investigation of the In Situ Formation of Nanocomposites

Interestingly, FTIR spectroscopy and TG-MS analysis suggested that $NiCl_2$ may produce a Ni nitride as a consequence of potential interactions with ($(\equiv Si)_3N$:) or N-H bonds; a Ni nitride compound was not detected as an intermediate by the XRD analysis (Figure 3). Within this context, we conducted further investigation focused on the **0.05NiPHPS** sample, the intermediate states (**Ni/SiN200** and **Ni/SiN300** samples) and the Ni/a-SiN nanocomposite (**Ni/SiN400** sample) and obtained a clear understanding of the in situ formation pathway by the Raman spectroscopic analysis (Figure 4).

The spectra have been recorded for the samples at polymer state as well as those listed in Table 1. At polymer state (**0.05NiPHPS** sample), the spectrum presents two sharp peaks at 169.4 cm^{-1} and 265.1 cm^{-1}, which are slightly red-shifted against those of as-received $NiCl_2$ at 171.0 cm^{-1} and 266.6 cm^{-1} shown in Figure S2 and one additional distinct peak centered at 503.3 cm^{-1} assigned to a Si-Si bond [39,40]. After pyrolysis at 200 °C (**Ni/SiN200** sample), the two peaks due to $NiCl_2$ further red-shifted to 168.8 cm^{-1} and 263.9 cm^{-1}, respectively.

Feshin et al. reported that the coordination of $N(CH_3)_3$ to $GeCl_4$ causes the electron density redistribution to elongate the Ge-Cl bond length and increase the polarity of the Ge-Cl bond [41]. It is generally accepted that the red-shifts of Raman peaks can be interpreted as a decrease in the force constant of chemical bonds, since the frequency is proportional to the square root of the force constant [42]. Therefore, it could be analogically assumed that the N:→Ni dative bond formation makes the Ni-Cl bond of $NiCl_2$ weaker and more polar and, hence, more reactive.

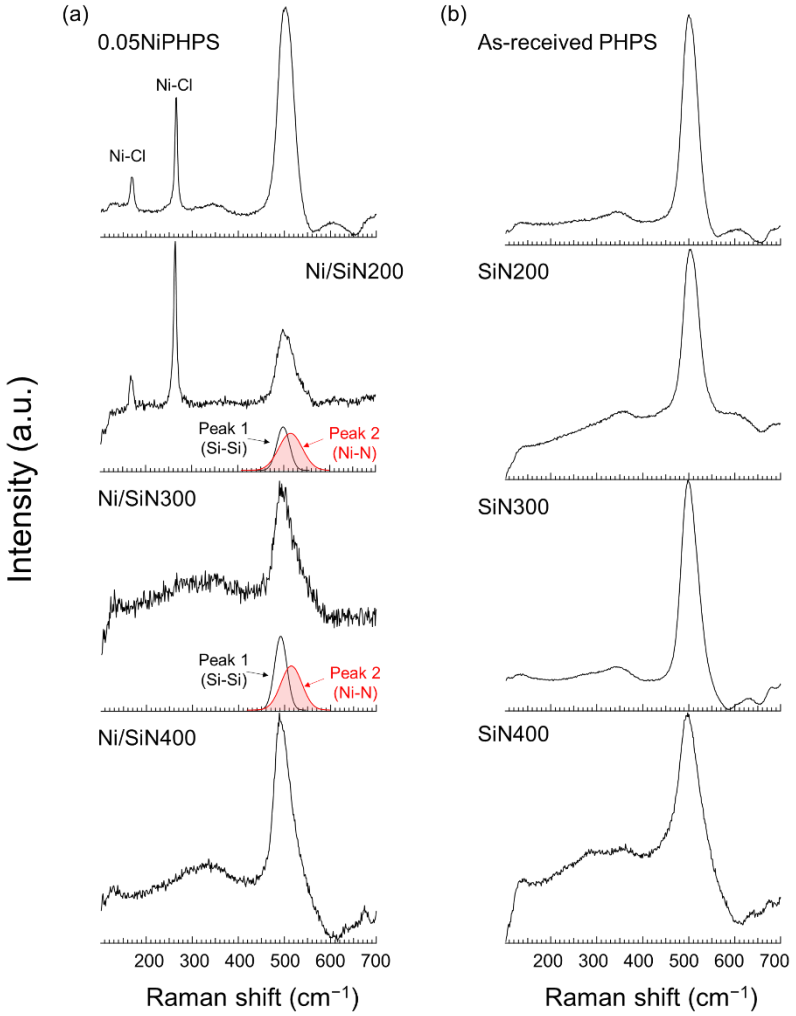

Figure 4. Raman spectra of (**a**) **0.05NiPHPS** and **Ni/SiNX** and (**b**) as-received PHPS and **SiNX** samples. Deconvolution by the Gaussian curve fitting performed on the broad peak around 500 cm^{-1} detected for the **Ni/SiN200** and **Ni/SiN300** samples yielded two peaks centered at 495 and 515 cm^{-1} labeled as **Peak 1** and **Peak 2**, respectively.

Meanwhile, the peak at 503.3 cm^{-1} became broader in the **Ni/SiN200** sample. The deconvolution of the broad signal yields the Si-Si bond peak centered at 498.7 cm^{-1} (**peak 1**) and an additional one at 514.8 cm^{-1} (**peak 2**) assigned to Ni-N bond in Ni_3N [43]. At 300 °C (**Ni/SiN300** sample), the two peaks due to $NiCl_2$ disappear and the peak area ratio of **peak 2**/**peak 1** decreases from 1.58 (**Ni/SiN200** sample) to 1.02 (**Ni/SiN300** sample), then at 400 °C, the **peak 2**, attributed to the Ni-N bond, disappears and the **Ni/SiN400** sample presents the **peak 1,** due to the Si-Si bond, as a single peak (Figure 4a). It should be noted that Raman spectrum of the **Ni/SiN400** sample in the wider Raman shift range is free from typical peaks attributed to amorphous silicon oxides such as Si-O-Si (820 cm^{-1}) and Si-$(OH)_x$ (920 and 1079 cm^{-1}) [44], while other peaks are found to correspond to the Raman peaks detected for SiN400 and thus attributed to PHPS-derived Si-N matrix networks (Figure S4). These results are consistent with the result of elemental analysis, showing that oxygen impurity is very low in both samples.

Under the present pyrolysis condition up to 400 °C, it is important to note that $NiCl_2$ keeps its initial state without thermal decomposition (Figure S5). Thus, the results obtained by the TG-MS, XRD, and Raman spectroscopic analyses reveal that the reaction of the activated $NiCl_2$ with PHPS begins to start below 200 °C and the subsequent metal Ni nucleation and crystallization occurs between 200 to 300 °C. Moreover, it is strongly suggested that

the in situ formation of metal Ni proceeds via the formation of Ni nitride species as intermediates. The Raman spectroscopic analysis reveals that Ni_3N is one possible intermediate phase (Figure 4a), which is well consistent with the reported thermodynamic data: Ni_3N has the lowest formation energy of NiN_x (x = 0 to 1/3) [45] and is a thermodynamically favorable phase at lower temperatures in the phase diagram for Ni-N system [46].

Regarding the Ni-N bond formation, since the temperature range detected by the Raman spectroscopic analysis was as low as 200 to 300 °C, the direct nitridation of Ni by atmospheric N_2 is excluded. Therefore, the Ni-N bond is intrinsically formed by the chemical reaction of $NiCl_2$ with PHPS as the nitrogen source via ternary silylamino groups.

It should be noted that the formation of Si-Si bond is reasonable since the N/Si atomic ratio of all the **Ni/SiNX** samples is lower than 1 (Table 1); indeed, all the **SiNX** samples with the N/Si atomic ratio <1 (Table 1) exhibited the typical Raman peak attributed to Si-Si bond (Figure 4b).

Based on these results, reactions during the polymer to metal Ni/a-SiN conversion process can be suggested as follows (Scheme 2): After the chemical modification of PHPS with $NiCl_2$ to afford Ni complexes (**1**), Ni-N bond formation would proceed via the nucleophilic attack of N atom of the silylamino group on the center Ni(II) cation to replace Cl. Since the N:→Ni dative bond has been already formed, the N atom would be easily accessible to Ni(II), and thus a S_N2 reaction via the transition state (**2**) is proposed. Subsequently, the nucleophilic attack of the released chloride anion (Cl^-) on other electrophiles, such as Si center of PHPS moieties (**3**), would proceed, leading to the evolution of monochlorosilane, as detected by the TG-MS analysis. Then, the formation of Ni nitride species (**5**) could proceed through the thermal decomposition of in situ preformed species, having Ni-N bond (**4**).

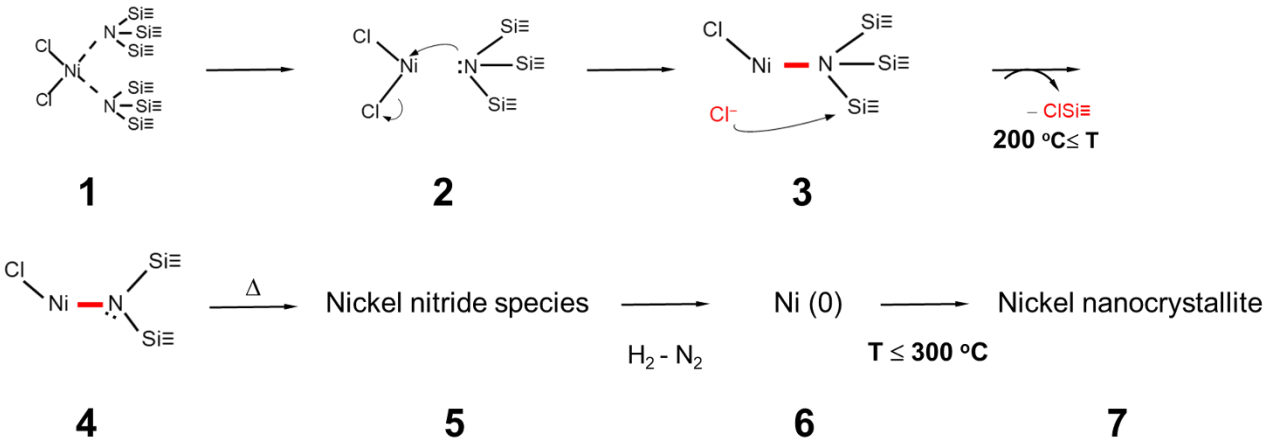

Scheme 2. Reaction scheme suggested for in situ formation of nickel nanocrystallite: Pre-formed Ni (II) complex (**1**) offers the nucleophilic attack of N atom of the silylamino group on the center Ni(II) cation to replace Cl (**2**). Subsequently, Ni-N bond formation proceeds accompanied by the attack of the released chloride anion (Cl^-) on other electrophiles, such as Si center of PHPS moieties (**3**). The resulting species with a Ni-N bond (**4**) decompose to give nickel nitride species (a possible one is Ni_3N) (**5**). Subsequent decomposition of (**5**) is facilitated by an in situ-formed H_2 leads to the formation of Ni (0) (**6**), followed by the nucleation and crystallization of Ni (**7**) at 200 to 300 °C.

In general, under N_2 or NH_3 atmosphere, Ni_3N, which is considered as the possible intermediate in this work, starts decomposing thermally at about 400 °C, accompanied by the formation of metallic Ni and gaseous nitrogen, while the Ni_3N decomposition temperature has been found to be as low as 157 °C due to its chemical fragility under an H_2 atmosphere [47,48]. Thus, it could be speculated that the local hydrogen partial pressure around the Ni nitride species embedded within the polymer-derived amorphous Si-N network reached a sufficiently high level to promote the immediate decomposition of the Ni nitride species (**5**), followed by the nucleation and subsequent crystallization of metal

Ni at 200 to 300 °C, shown as (**6**) and (**7**) in Scheme 2. As previously mentioned, $NiCl_2$ exhibited high catalytic activity to facilitate Si-H/N-H dehydrocoupling reactions in PHPS moieties. It should be noted that this $NiCl_2$-catalyzed dehydrocoupling reaction proceeded contentiously during pyrolysis, which facilitated the polymer to the ceramic conversion of PHPS up to 400 °C.

In addition, the transamination reaction leads to the formation of the byproducts, NH_4NiCl_3 and NH_4Cl, as shown in Figure 3, resulting from the nucleation reactions of the gaseous NH_3 formed in situ with Ni complexes and the NH_3 with HCl formed in situ, respectively. Then, above 300 °C, the byproducts thermally decompose to yield gaseous NH_3 and HCl, while the regenerated $NiCl_2$ species would participate in the Ni-N bond formation reaction as shown in Scheme 2.

To assess the phase nanostructure of the metal Ni/amorphous silicon nitride composites in more detail, TEM observation was performed on the **Ni/SiN400** sample. As shown in Figure 5a, many dark dots correspond to metallic Ni crystallites embedded within amorphous silicon nitride matrix. In fact, the fringe spacing calculated from Figure 5b is found to be 0.125 nm, 0.177 nm, and 0.202 nm, corresponding to the (220), (200), and (111) lattice planes of fcc Ni (JCPDS No. 01-070-1849), respectively.

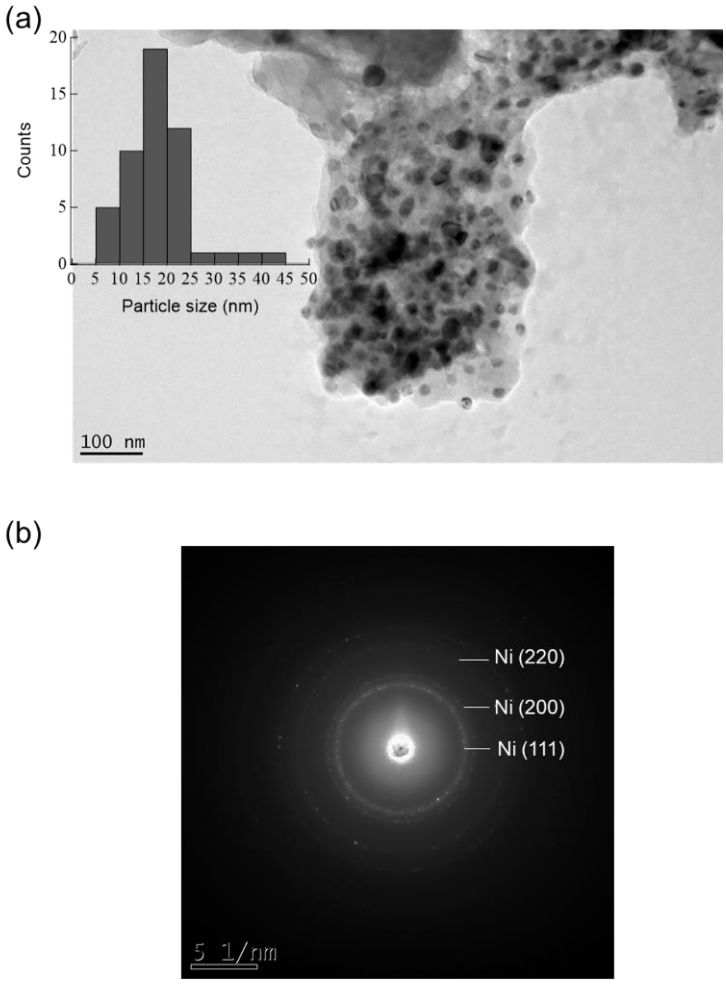

Figure 5. *Cont.*

(c)

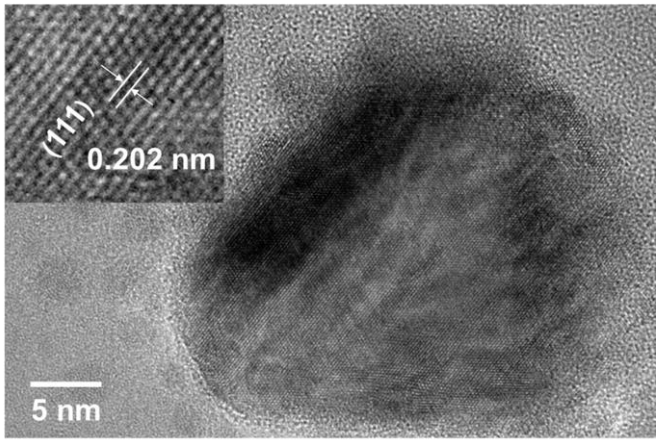

Figure 5. (**a**) TEM image of **Ni/SiN400** sample showing Ni nanocrystallites formed in situ within amorphous silicon nitride matrix and inset presenting a size distribution histogram (statistics on 50 Ni nanocrystallites) measured by TEM, (**b**) a selected area electron diffraction pattern obtained for the **Ni/SiN400** sample, and (**c**) a high-resolution image with the enlarged one (inset).

A brief size distribution analysis by measuring the size of 50 Ni nanocrystallites revealed a relatively wide range of size distribution from 7.32 to 43.4 nm; however, most of the Ni crystallites were below 25 nm in size, and the mean size was found as 18.0 nm. This is confirmed by the high-resolution image (Figure 5c) which reveals the presence of a nanocrystal with a lattice spacing of 0.202 nm, corresponding to the *d*-spacing of the lattice plane of the Ni structure, i.e., the (111) direction of the *fcc* cubic Ni structure which agrees with the phase identified, as well in the X-ray diffractogram (Figure 3), as seen in the SAED pattern (Figure 5b) of the same sample.

4. Conclusions

In this study, we reported on the in situ formation of metallic nickel nanocrystallites, with an average Ni size of 18.0 nm, finely dispersed within a polymer-derived amorphous silicon nitride matrix at pyrolysis temperatures as low as 400 °C. The results can be summarized as follows:

1. ATR-FTIR spectroscopic analysis revealed that $NiCl_2$ had high catalytic activity for dehydrocoupling reactions between Si-H and N-H of PHPS under the present precursor synthesis condition conducted in toluene at reflux (~110 °C), leading to the formation of ternary silylamino groups ($(\equiv Si)_3N$:). Consequently, the ternary silylamino group coordinated the Ni(II) cation of $NiCl_2$ to afford a complex such as the 4-coordinated Ni(II) complex.
2. TG-MS and Raman spectroscopic analyses revealed that the Ni-N bond in Ni nitride species is intrinsically formed via the S_N2 reaction of the preformed 4-coordinated Ni(II) complex at 200 °C: the nucleophilic attack of the N atom of the silylamino group on the center Ni(II) cation and simultaneous elimination of Cl^- as a leaving group. Subsequently, the nucleophilic attack of the released Cl^- on other electrophiles, such as Si center of PHPS moieties, would proceed accompanied by the evolution of monochlorosilane, while the N-bonded Ni species subsequently decomposed to give the Ni nitride species.
3. XRD, ATR-FTIR, and Raman spectroscopic analyses revealed that Ni nanocrystallites started to form at temperatures as low as 200 to 300 °C through the decomposition reaction of the in situ formed Ni nitride species facilitated by H_2, which was generated through the $NiCl_2$-catalyzed dehydrocoupling reaction of PHPS. In addition, this $NiCl_2$-catalyzed dehydrocoupling reaction of PHPS accelerated the polymer to the ceramic conversion of PHPS up to 400 °C.

Therefore, it can be concluded that the low temperature in situ formation of Ni/amorphous silicon nitride composites was governed by the synergistic effect of the following two reactions attributed to the high catalytic performance of $NiCl_2$ for dehydrocoupling reaction of PHPS: (i) the Ni(II) complex formation allows in situ formation of the Ni nitride species as an intermediate below 200 °C and (ii) the immediate decomposition of the Ni nitride species promotes Ni nucleation at 200 to 300 °C.

Based on our results obtained in this study, it is highly expected that the ability to control material properties such as the size of Ni nanocrystallites, chemical composition, and pore size distribution by designing polymeric precursors can be achieved.

Thus, further investigation on the molecular structure of single source precursors for the ideal metal/nitride nanocomposites is in progress and the nanocomposites are expected to be applied as a new, highly active catalyst for important reactions, such as the hydrogenation of CO_2, which is a promising way to solve the environmental and energy affairs caused by CO_2 emissions. Such a study is under investigation and will be published separately.

Supplementary Materials: The following supporting information can be downloaded at: https://www.mdpi.com/article/10.3390/nano12101644/s1, Table S1: Intensity ratio of typical IR absorption bands for as-received PHPS and Ni-modified PHPS samples; Figure S1: TG-MS analysis under flowing He of the as-received PHPS sample; Figure S2: Powder X-ray diffraction patterns of pure $NiCl_2$ and pure $NiCl_2$ after pyrolysis at 300 °C under reductive gases (NH_3 and 10% H_2); Figure S3: Raman spectrum of pure $NiCl_2$; Figure S4: Raman spectra of Ni/SiN400 (black line) and SiN400 (red line) in a wider Raman shift range; Figure S5: Powder X-ray diffraction patterns of $NiCl_2$ after pyrolysis at 200, 300, and 400 °C under the same manner for the pyrolysis of **0.05NiPHPS**.

Author Contributions: N.A., S.T. conceived and planned this study and drafted the manuscript; E.K., S.H. and M.T. contributed to the evaluation of samples; P.C. took and discussed the TEM images; R.K.N. and S.B. reviewed the draft; Y.I. conceived, reviewed, and supervised this work. All authors have read and agreed to the published version of the manuscript.

Funding: This research was funded by JSPS KAKENHI, Grant Number JP20K05076, and CNRS via the International Research Project (IRP) 'Ceramics materials for societal challenges'. The APC was funded by JST SPRING, Grant Number JPMJSP2112.

Institutional Review Board Statement: Not applicable.

Informed Consent Statement: Not applicable.

Data Availability Statement: The data reported in this study are available from the authors upon reasonable request.

Acknowledgments: Norifumi Asakuma acknowledges receiving financial support from JST SPRING, Grant Number JPMJSP2112.

Conflicts of Interest: The authors declare no conflict of interest.

References

1. Marakatti, V.S.; Gaigneaux, E.M. Recent Advances in Heterogeneous Catalysis for Ammonia Synthesis. *ChemCatChem* **2020**, *12*, 5838–5857. [CrossRef]
2. Aziz, M.A.A.; Jalil, A.A.; Triwahyono, S.; Ahmad, A. CO_2 Methanation over Heterogeneous Catalysts: Recent Progress and Future Prospects. *Green Chem.* **2015**, *17*, 2647–2663. [CrossRef]
3. Sudarsanam, P.; Zhong, R.; van Den Bosch, S.; Coman, S.M.; Parvulescu, V.I.; Sels, B.F. Functionalised Heterogeneous Catalysts for Sustainable Biomass Valorisation. *Chem. Soc. Rev.* **2018**, *47*, 8349–8402. [CrossRef] [PubMed]
4. Gielen, D.; Boshell, F.; Saygin, D. Climate and Energy Challenges for Materials Science. *Nat. Mater.* **2016**, *15*, 117–120. [CrossRef]
5. Colombo, P.; Mera, G.; Riedel, R.; Sorarù, G.D. Polymer-Derived Ceramics: 40 Years of Research and Innovation in Advanced Ceramics. *J. Am. Ceram. Soc.* **2010**, *93*, 1805–1837. [CrossRef]
6. Iwamoto, Y.; Motz, G.; Ionescu, E.; Bernard, S. Preceramic Polymers as Precursors of Advanced Ceramics: The Polymer-Derived Ceramics (PDCs) Route. *Encycl. Mater. Tech. Ceram. Glas.* **2021**, *1*, 93–102. [CrossRef]
7. Viard, A.; Fonblanc, D.; Lopez-Ferber, D.; Schmidt, M.; Lale, A.; Durif, C.; Balestrat, M.; Rossignol, F.; Weinmann, M.; Riedel, R.; et al. Polymer Derived Si–B–C–N Ceramics: 30 Years of Research. *Adv. Eng. Mater.* **2018**, *20*, 1–31. [CrossRef]

8. Zaheer, M.; Hermannsdörfer, J.; Kretschmer, W.P.; Motz, G.; Kempe, R. Robust Heterogeneous Nickel Catalysts with Tailored Porosity for the Selective Hydrogenolysis of Aryl Ethers. *ChemCatChem* **2014**, *6*, 91–95. [CrossRef]
9. Schumacher, D.; Wilhelm, M.; Rezwan, K. Porous SiOC Monoliths with Catalytiac Activity by in Situ Formation of Ni Nanoparticles in Solution-Based Freeze Casting. *J. Am. Ceram. Soc.* **2020**, *103*, 2991–3001. [CrossRef]
10. Bazarjani, M.S.; Kleebe, H.J.; Müller, M.M.; Fasel, C.; Yazdi, M.B.; Gurlo, A.; Riedel, R. Nanoporous Silicon Oxycarbonitride Ceramics Derived from Polysilazanes in Situ Modified with Nickel Nanoparticles. *Chem. Mater.* **2011**, *23*, 4112–4123. [CrossRef]
11. Forberg, D.; Schwob, T.; Kempe, R. Catalytic Condensation for the Formation of Polycyclic Heteroaromatic Compounds. *Nat. Commun.* **2018**, *9*, 1751. [CrossRef] [PubMed]
12. Forberg, D.; Schwob, T.; Zaheer, M.; Friedrich, M.; Miyajima, N.; Kempe, R. Single-Catalyst High-Weight% Hydrogen Storage in an N-Heterocycle Synthesized from Lignin Hydrogenolysis Products and Ammonia. *Nat. Commun.* **2016**, *7*, 13201. [CrossRef] [PubMed]
13. Glatz, G.; Schmalz, T.; Kraus, T.; Haarmann, F.; Motz, G.; Kempe, R. Copper-Containing SiCN Precursor Ceramics (Cu@SiCN) as Selective Hydrocarbon Oxidation Catalysts Using Air as an Oxidant. *Chem. A Eur. J.* **2010**, *16*, 4231–4238. [CrossRef] [PubMed]
14. Zaheer, M.; Schmalz, T.; Motz, G.; Kempe, R. Polymer Derived Non-Oxide Ceramics Modified with Late Transition Metals. *Chem. Soc. Rev.* **2012**, *41*, 5102–5116. [CrossRef]
15. Forberg, D.; Obenauf, J.; Friedrich, M.; Hühne, S.M.; Mader, W.; Motz, G.; Kempe, R. The Synthesis of Pyrroles via Acceptorless Dehydrogenative Condensation of Secondary Alcohols and 1,2-Amino Alcohols Mediated by a Robust and Reusable Catalyst Based on Nanometer-Sized Iridium Particles. *Catal. Sci. Technol.* **2014**, *4*, 4188–4192. [CrossRef]
16. Hahn, G.; Ewert, J.K.; Denner, C.; Tilgner, D.; Kempe, R. A Reusable Mesoporous Nickel Nanocomposite Catalyst for the Selective Hydrogenation of Nitroarenes in the Presence of Sensitive Functional Groups. *ChemCatChem* **2016**, *8*, 2461–2465. [CrossRef]
17. Kamperman, M.; Burns, A.; Weissgraeber, R.; van Vegten, N.; Warren, S.C.; Gruner, S.M.; Baiker, A.; Wiesner, U. Integrating Structure Control over Multiple Length Scales in Porous High Temperature Ceramics with Functional Platinum Nanoparticles. *Nano Lett.* **2009**, *9*, 2756–2762. [CrossRef]
18. Sachau, S.M.; Zaheer, M.; Lale, A.; Friedrich, M.; Denner, C.E.; Demirci, U.B.; Bernard, S.; Motz, G.; Kempe, R. Micro-/Mesoporous Platinum–SiCN Nanocomposite Catalysts (Pt@SiCN): From Design to Catalytic Applications. *Chem. A Eur. J.* **2016**, *22*, 15508–15512. [CrossRef]
19. Schwob, T.; Kempe, R. A Reusable Co Catalyst for the Selective Hydrogenation of Functionalized Nitroarenes and the Direct Synthesis of Imines and Benzimidazoles from Nitroarenes and Aldehydes. *Angew. Chem. Int. Ed.* **2016**, *55*, 15175–15179. [CrossRef]
20. Bäumler, C.; Kempe, R. The Direct Synthesis of Imines, Benzimidazoles and Quinoxalines from Nitroarenes and Carbonyl Compounds by Selective Nitroarene Hydrogenation Employing a Reusable Iron Catalyst. *Chem. A Eur. J.* **2018**, *24*, 8989–8993. [CrossRef]
21. Chen, L.; Qi, Z.; Zhang, S.; Su, J.; Somorjai, G.A. Catalytic Hydrogen Production from Methane: A Review on Recent Progress and Prospect. *Catalysts* **2020**, *10*, 858. [CrossRef]
22. Frontera, P.; Macario, A.; Ferraro, M.; Antonucci, P.L. Supported Catalysts for CO_2 Methanation: A Review. *Catalysts* **2017**, *7*, 59. [CrossRef]
23. Kurzina, I.; Aires, F.J.C.S.; Bergeret, G.; Bertolini, J.C. Total Oxidation of Methane over Pd Catalysts Supported on Silicon Nitride: Influence of Support Nature. *Chem. Eng. J.* **2005**, *107*, 45–53. [CrossRef]
24. Shang, R.; Sun, W.; Wang, Y.; Jin, G.Q.; Guo, X.Y. Silicon Nitride Supported Nickel Catalyst for Partial Oxidation of Methane to Syngas. *Catal. Commun.* **2008**, *9*, 2103–2106. [CrossRef]
25. Aires, F.J.C.S.; Bertolini, J.C. On the Use of Silicon Nitride in Catalysis. *Top. Catal.* **2009**, *52*, 1492–1505. [CrossRef]
26. Yan, L.; Liu, J.; Wang, X.; Ma, C.; Zhang, C.; Wang, H.; Wei, Y.; Wen, X.; Yang, Y.; Li, Y. Ru Catalysts Supported by Si_3N_4 for Fischer-Tropsch Synthesis. *Appl. Surf. Sci.* **2020**, *526*, 146631. [CrossRef]
27. Lale, A.; Mallmann, M.D.; Tada, S.; Bruma, A.; Özkar, S.; Kumar, R.; Haneda, M.; Machado, R.A.F.; Iwamoto, Y.; Demirci, U.B.; et al. Highly Active, Robust and Reusable Micro-/Mesoporous TiN/Si3N4 Nanocomposite-Based Catalysts for Clean Energy: Understanding the Key Role of TiN Nanoclusters and Amorphous Si3N4 Matrix in the Performance of the Catalyst System. *Appl. Catal. B Environ.* **2020**, *272*, 118975. [CrossRef]
28. Hullmann, D.; Wendt, G.; Ziegenbalg, G. Porous Silicon Nitride Materials as Basic Catalysts. *Chem. Eng. Technol.* **2001**, *24*, 147–150. [CrossRef]
29. Lale, A.; Proust, V.; Bechelany, M.C.; Viard, A.; Malo, S.; Bernard, S. A Comprehensive Study on the Influence of the Polyorganosilazane Chemistry and Material Shape on the High Temperature Behavior of Titanium Nitride/Silicon Nitride Nanocomposites. *J. Eur. Ceram. Soc.* **2017**, *37*, 5167–5175. [CrossRef]
30. Balestrat, M.; Lale, A.; Bezerra, A.V.A.; Proust, V.; Awin, E.W.; Machado, R.A.F.; Carles, P.; Kumar, R.; Gervais, C.; Bernard, S. In-Situ Synthesis and Characterization of Nanocomposites in the Si-Ti-N and Si-Ti-C Systems. *Molecules* **2020**, *25*, 5236. [CrossRef]
31. Zhou, C.; Ott, A.; Ishikawa, R.; Ikuhara, Y.; Riedel, R.; Ionescu, E. Single-Source-Precursor Synthesis and High-Temperature Evolution of Novel Mesoporous SiVN(O)-Based Ceramic Nanocomposites. *J. Eur. Ceram. Soc.* **2020**, *40*, 6280–6287. [CrossRef]
32. Tada, S.; Mallmann, M.D.; Takagi, H.; Iihama, J.; Asakuma, N.; Asaka, T.; Daiko, Y.; Honda, S.; Nishihora, R.K.; Machado, R.A.F.; et al. Low Temperature in Situ formation of Cobalt in Silicon Nitride toward Functional Nitride Nanocomposites. *Chem. Commun.* **2021**, *57*, 2057–2060. [CrossRef] [PubMed]

33. Scardera, G.; Puzzer, T.; Conibeer, G.; Green, M.A. Fourier Transform Infrared Spectroscopy of Annealed Silicon-Rich Silicon Nitride Thin Films. *J. Appl. Phys.* **2008**, *104*, 104310. [CrossRef]
34. Hasegawa, S.; Matsuda, M.; Kurata, Y. Si-H and N-H Vibrational Properties in Glow-Discharge Amorphous SiNx:H Films ($0 < x < 1.55$). *Appl. Phys. Lett.* **1990**, *57*, 2211–2213. [CrossRef]
35. Clark, T.J.; Lee, K.; Manners, I. Transition-Metal-Catalyzed Dehydrocoupling: A Convenient Route to Bonds between Main-Group Elements. *Chem.-A Eur. J.* **2006**, *12*, 8634–8648. [CrossRef]
36. Lucovsky, G.; Yang, J.; Chao, S.S.; Tyler, J.E.; Czubatyj, W. Nitrogen-Bonding Environments in Glow-Discharge Deposited a-Si:H Films. *Phys. Rev. B* **1983**, *28*, 3234–3240. [CrossRef]
37. Yive, S.C.K.; Corriu, R.J.P.; Leclercq, D.; Mutin, P.H.; Vioux, A. Thermogravimetric Analysis/Mass Spectrometry Investigation of the Thermal Conversion of Organosilicon Precursors into Ceramics under Argon and Ammonia. 2. Poly(silazanes). *Chem. Mater.* **1992**, *4*, 1263–1271. [CrossRef]
38. Yive, S.C.K.; Corriu, R.J.P.; Leclercq, D.; Mutin, P.H.; Vioux, A. Silicon Carbonitride from Polymeric Precursors: Thermal Cross-Linking and Pyrolysis of Oligosilazane Model Compounds. *Chem. Mater.* **1992**, *4*, 141–146. [CrossRef]
39. Loaiza, L.C.; Monconduit, L.; Seznec, V. Siloxene: A Potential Layered Silicon Intercalation Anode for Na, Li and K Ion Batteries. *J. Power Sources* **2019**, *417*, 99–107. [CrossRef]
40. Periasamy, S.; Venkidusamy, S.; Venkatesan, R.; Mayandi, J.; Pearce, J.; Selj, J.H.; Veerabahu, R. Micro-Raman Scattering of Nanoscale Silicon in Amorphous and Porous Silicon. *Zeitschrift Phys. Chem.* **2017**, *231*, 1585–1598. [CrossRef]
41. Feshin, V.P.; Feshina, E.V. Nature of the Coordination Bond in the $GeCl_4$-Trimethylamine Complex. *Russ. J. Inorg. Chem.* **2014**, *59*, 1157–1161. [CrossRef]
42. Karki, B.; Freelon, B.; Rajapakse, M.; Musa, R.; Riyadh, S.S.M.; Morris, B.; Abu, U.O.; Yu, M.; Sumanasekera, G.U.; Jasinski, J.B. Strain-Induced Vibrational Properties of Few Layer Black Phosphorus and $MoTe_2$ via Raman Spectroscopy. *Nanotechnology* **2020**, *31*, 425707. [CrossRef] [PubMed]
43. Zhang, N.; Zou, Y.; Tao, L.; Chen, W.; Zhou, L.; Liu, Z.; Zhou, B.; Huang, G.; Lin, H.; Wang, S. Electrochemical Oxidation of 5-Hydroxymethylfurfural on Nickel Nitride/Carbon Nanosheets: Reaction Pathway Determined by In Situ Sum Frequency Generation Vibrational Spectroscopy. *Angew. Chem.* **2019**, *131*, 16042–16050. [CrossRef]
44. Mueller, T.; Schwertheim, S.; Fahrner, W.R. Crystalline Silicon Surface Passivation by High-Frequency Plasma-Enhanced Chemical-Vapor-Deposited Nanocomposite Silicon Suboxides for Solar Cell Applications. *J. Appl. Phys.* **2010**, *107*, 014504. [CrossRef]
45. Fang, C.M.; Sluiter, M.H.F.; Van Huis, M.A.; Zandbergen, H.W. Structural and Magnetic Properties of NiC x and NiN x (X = 0 to 13) Solid Solutions from First-Principles Calculations. *Phys. Rev. B-Condens. Matter Mater. Phys.* **2012**, *86*, 134114. [CrossRef]
46. Neklyudov, I.M.; Morozov, A.N. Formation and Decay Kinetics of Nickel Nitrides Resulting from Nitrogen Ion Implantation. The Nickel-Nitrogen Phase Diagram. *Phys. B Condens. Matter* **2004**, *350*, 325–337. [CrossRef]
47. Gage, S.H.; Trewyn, B.G.; Ciobanu, C.V.; Pylypenko, S.; Richards, R.M. Synthetic Advancements and Catalytic Applications of Nickel Nitride. *Catal. Sci. Technol.* **2016**, *6*, 4059–4076. [CrossRef]
48. Baiker, A.; Maciejewski, M. Formation and Thermal Stability of Copper and Nickel Nitrides. *J. Chem. Soc. Faraday Trans. Phys. Chem. Condens. Phases* **1984**, *80*, 2331–2341. [CrossRef]